PERGAMON

Journal of Structural Geology 24 (2002) 763–772

JOURNAL OF STRUCTURAL GEOLOGY

www.elsevier.com/locate/jstrugeo

# Kinematic and analog modeling of 3-D extensional ramps: observations and a new 3-D deformation model

Donald A. Medwedeff*, Robert W. Krantz[1]

*ARCO Exploration and Production Technology, 2300 West Plano Parkway, Plano, TX 75075, USA*

Received 7 September 2000; revised 17 January 2001; accepted 30 May 2001

**Abstract**

We present results of kinematic and dry-sand analog models of hanging wall folding over an extensional ramp–flat system containing complementary strike bends. The kinematic models illustrate that differential structural relief is controlled by changes in apparent fault dip in the displacement direction. Variation in 'inclined-shear' angle modifies the magnitude, but not the sign, of this differential relief.

In a novel analog modeling method, we create a weak fault zone by coating the entire rigid footwall (ramps and flat) with a thin layer of silicone putty below a dry sand hanging wall. At low strain rates, the silicone polymer is weaker than the dry sand and thus provides a good fault zone analog. A 3° tilt is sufficient to induce displacement, and all deformation is driven by gravity. In the models, we observe that hanging wall displacements near the oblique segment of the ramp are deflected toward the ramp strike.

Oblique inclined-shear, a new quantitative geometric model, explains the bending of displacement paths towards the strike, rather than the dip, of oblique ramp segments. The model is conceptually equivalent to 2-D, inclined-shear models in which the hanging wall is imagined to pull rigidly away from and then collapse against the footwall. Because gravity is the driving force, antithetic collapse is directed normal to the incipient void, which introduces a component of slip normal to the fault strike. Vector sum of the normal component with the regional component results in the observed displacement. 

*Keywords*: Kinematic model; Analog model; Extensional ramp

## 1. Introduction

Inclined shear is a conceptual deformation mechanism in which folding is accommodated by simple-shear along parallel, inclined shear planes (Fig. 1). The inclined shear concept has been extensively used to model extensional fault-related folds (White et al., 1986; Dula, 1991; Kerr and White, 1992; Xiao and Suppe, 1992). Folding strain in most cases is distributed over a network of variably oriented faults. Yet motion on these faults can often be approximated by slip on *effective* shear planes with a single orientation. The value of inclined-shear modeling is that it provides a simple, yet quantitative approximation for relating hanging wall fold geometry and kinematics to fault shape (White et al., 1986; Dula, 1991; Kerr and White, 1992).

The majority of studies evaluating inclined shear have taken a 2-D approach (cross-sectional), with the cross-section being parallel to the fault dip and displacement direction. The third dimension is a cylindrical projection of the fault and fold along strike. However, a few studies have evaluated the inclined-shear model in 3-D (Xiao and Dula, 1989; Kerr et al., 1993; Braun et al., 1994). These studies model curved or doubly curved fault surfaces. This smooth curvature creates complex hanging wall folding, which we believe masks the fundamental processes (Kerr et al., 1993; Braun et al., 1994).

We present results of kinematic and analog model experiments to test the degree of validity of inclined-shear theory in non-cylindrical 3-D applications. We model an angular ramp–flat extensional fault with complementary angular strike bends (Fig. 2). This simple geometry isolates the deformation effects of the fault bends. As in the case of 2-D fault-bend folding (Suppe, 1983), isolating these effects fosters insight into deformation processes and simplifies quantitative analysis.

This paper is presented in three sections. First, we use kinematic models to show unambiguously the relationship between boundary conditions, deformation mechanisms, and displacements. Second, we present analog model results which document systematic 3-D displacement patterns over

* Corresponding author. Present address: ChevronTexaco Exploration and Production Technology Company, 6001 Bollinger Canyon Rd., San Ramon, CA 94583, USA. Tel.: +1-925-842-6346.

*E-mail address:* dmedwedeff@chevrontexaco.com (D.A. Medwedeff).

[1] Present address: Phillips Alaska Inc., 700 G Street Anchorage, AK 99507, USA.

0191-8141/02/$ - see front matter 
PII: S0191-8141(01)00121-3

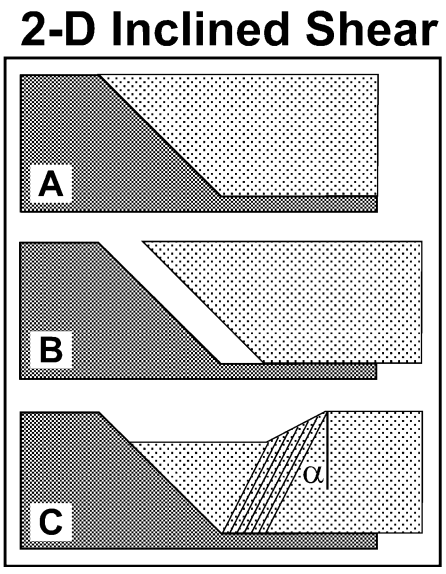


Fig. 1. Schematic illustration of 2-D inclined shear. Deformable hanging wall (A) is extended from a rigid footwall (B). During extension, the hanging wall deforms by shear antithetic to the dipping ramp.

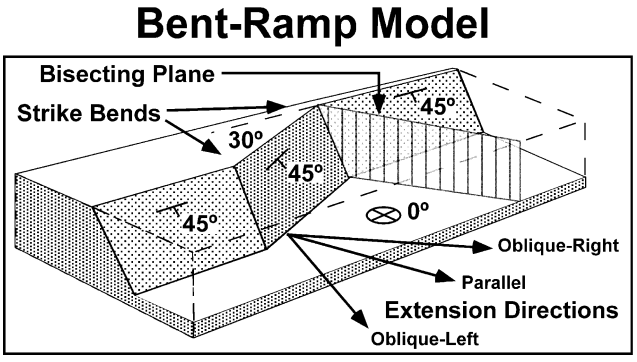


Fig. 2. Bent-ramp model used to evaluate the validity of inclined shear models for 3-D structures. Angular fault bends serve to localize the strain effects of the non-cylindrical fault geometry.

oblique fault ramps. Finally, we present a geometric theory that generalizes inclined shear to three dimensions and explains the observed displacements.

## 2. Kinematic models

Though dramatically simpler than nature, analog model results are affected by a variety of material and mechanical complexities, which are not fully controlled. Therefore, using GeoSec3D®, we performed a series of kinematic models to form a baseline for analyzing the analog model results. These models use a strict homogeneous, pencil-shear deformation mechanism. This means that particles are displaced by a constant heave, and then moved differentially along *parallel* paths to maintain constant volume. Because of its simplicity, pencil-shear deformation provides an end-member result with which to compare the analog results.

### 2.1. Model parameters

The pencil-shear technique has two variable parameters: the extension direction and the inclined-shear angle (Kerr and White, 1992). We use three values of each for a total of nine models (Table 1 and Fig. 3). The fault geometry comprises steep ramps with angular bends above a horizontal 'regional' detachment. Two 'normal' ramps parallel the model boundary. Between them lies an 'oblique' ramp, providing both a convex and a concave strike bend. For the baseline case, we set the extension direction parallel to the line of intersection of the normal and oblique fault ramps. The other two cases allow the extension direction to deviate towards the dip direction of the normal ramps and towards the dip direction of the oblique ramp. The inclined shear angle is set to 20° antithetic, vertical, and 20° synthetic to the normal fault ramp. By design, the shear direction is always contained in planes parallel to the extension.

### 2.2. Results

Fault geometry and displacement magnitude are constant for all the models. Nonetheless, variation in shear angle and displacement direction produces clear variations in the resulting horizon geometry (Fig. 3).

For convenience we refer to models in which the slip direction bisects the map-view bend in the ramp as having symmetric displacement. Similarly we say that models in which the slip direction is clockwise of the ramp-bend bisecting angle have clockwise displacement and that models in which the slip direction is counter-clockwise of the ramp-bend bisecting angle have counter-clockwise displacement. Note that these designations are arbitrary and tied to the asymmetry of our model.

In symmetric models (d, e, and f) the oblique ramp

Table 1
Specified displacement directions and inclined-shear angles for the nine kinematic models

| | | Inclined-shear angle | | |
|---|---|---|---|---|
| | | 20° Antithetic | Vertical | 20° Synthetic |
| Displacement direction | Clockwise | Model a | Model b | Model c |
| | Symmetric | Model d | Model e | Model f |
| | Counter-clockwise | Model g | Model h | Model i |

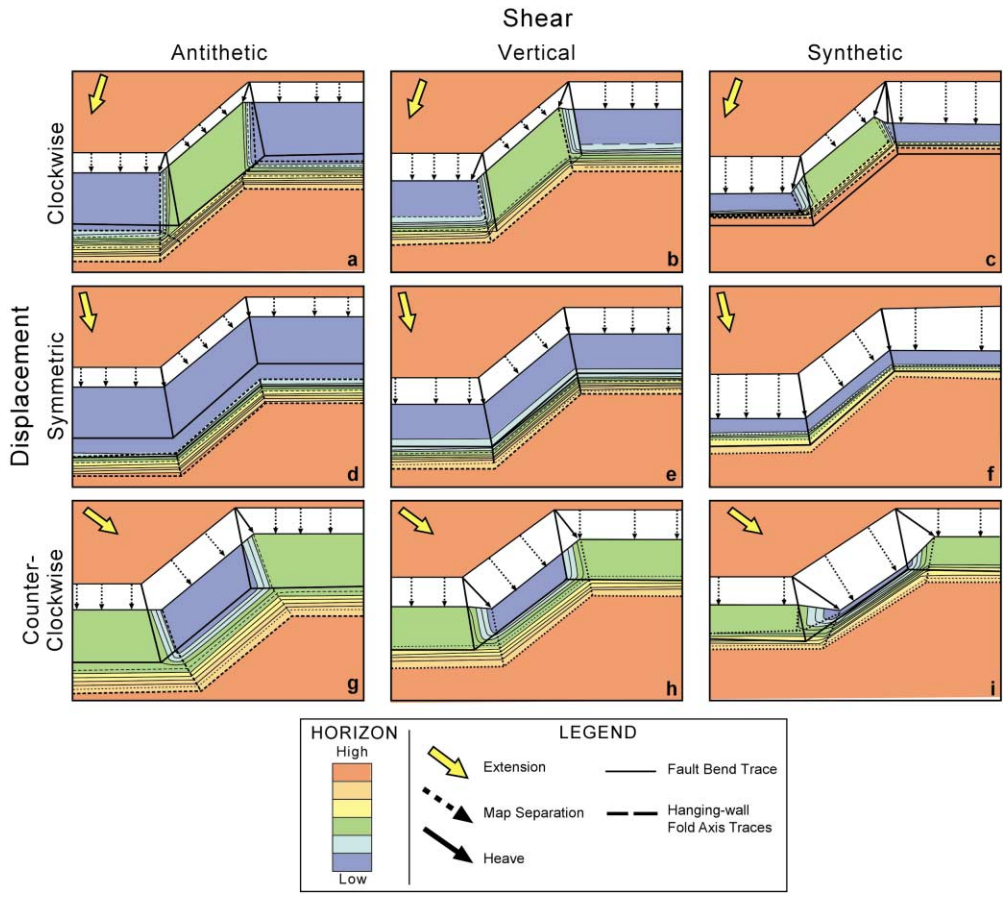


Fig. 3. Gray-scale structural-contour maps for the results of nine kinematic models of extension over oblique ramps. Units are arbitrary. The nine models represent the different permutations of synthetic, vertical, and antithetic inclined shear combined with clockwise, symmetric, and counter-clockwise displacement. See text for discussion.

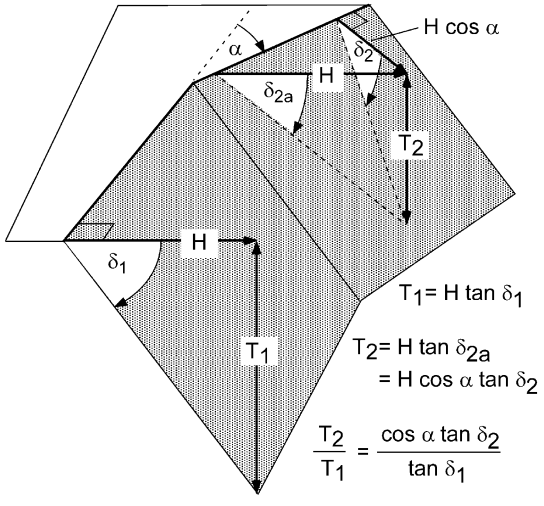


Fig. 4. Parameters for computing differential structural relief across differently striking fault ramps. For any given direction, the apparent dip of the two planes will be different and thus the structural relief will also differ. The one exception is the vertical plane containing the line of intersection of the two ramps.

generates no differential structural relief. Comparison of model d with model f shows that variation in the inclined-shear angle modifies the magnitude, but not the direction, of the fold axis.

In clockwise models (a, b, and c) the oblique ramp generates positive structural relief relative to the lateral segments. Comparison of model a with model c shows that variation in the inclined-shear angle modifies the size, but not the overall map pattern, of the fold. Antithetic shear produces a broader, gentler fold. Synthetic shear produces a smaller, tighter fold.

In counter-clockwise models (g, h, and i) the oblique ramp generates negative structural relief relative to the lateral segments. Again, comparison of model a with model c shows that variation in the inclined-shear angle modifies the size, but not the general shape of fold. Antithetic shear produces a broader, gentler fold. Synthetic shear produces a smaller, tighter fold.

### 2.3. Analysis

The models show that differential structural relief is controlled by changes in apparent fault dip in the

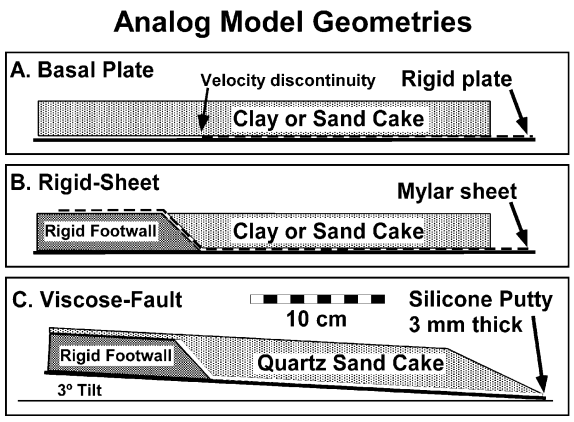


Fig. 5. Drive mechanisms and boundary conditions for extensional analog models. Note that the fault zone is stronger than the wall rock in both the flexible sheet and the rigid basement techniques. In contrast, the silicone-putty fault zone is substantially weaker than the wall rock and deformation occurs with only a 3° slope.

displacement direction. Given the assumptions of inclined shear, this phenomena is purely geometric and is described by:

$$T_2/T_1 = (\cos\alpha\tan\delta_2)/\tan\delta_1 \quad (1)$$

As shown in Fig. 4, $T_1$ and $\delta_1$ are the throw and dip for a ramp perpendicular to the displacement direction, and $T_2$ and $\delta_2$ are the throw and dip for a ramp inclined $90 - \alpha$ degrees to the displacement direction. Along-strike changes in fault shape can thus generate structural highs and lows and provide lateral fold closure, in the presence of a regional dip.

Fault heave is sometimes used as a proxy for fault throw. However, comparison of the models shows that fault heave is a function of the local fault strike, inclined shear angle, and the displacement direction. Thus heave bears no clear relationship to the true slip. However, matching of characteristic shapes between hanging wall and footwall indicates the true slip. Conversely, complex variations in heave may indicate unrecognized changes in fault geometry or kinematics.

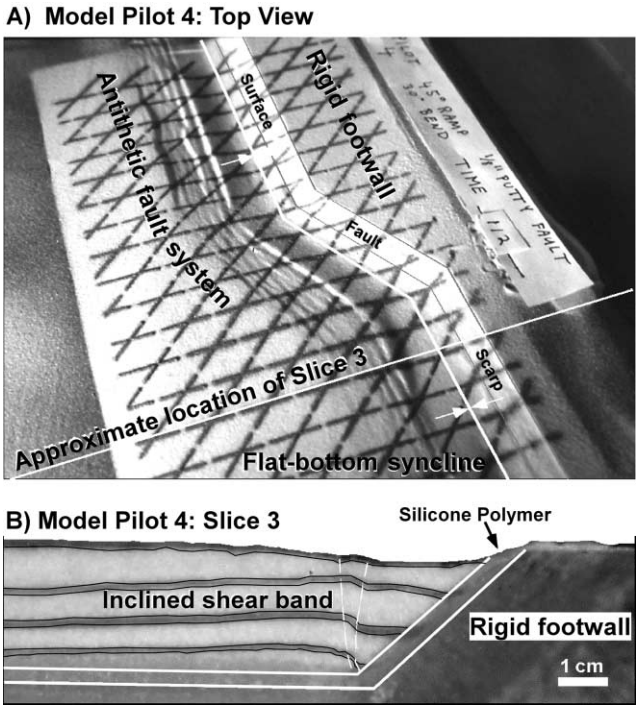


Fig. 6. (A) Oblique view of model Pilot 4 showing passive grid and surface deformation. Key features are: (1) the structural low formed over the fault ramp, and (2) the zone of localized faulting above the base of the fault ramp. (B) Cross-section view of model Pilot 4 showing passive sand above the silicone fault zone. Key features are: (1) the structural low formed over the fault ramp, and (2) the zone of localized faulting above the base of the fault ramp.

## 3. Analog models

### 3.1. Previous techniques

Most previous analog models of detached normal faults have used one of two driving mechanisms to induce extension on a low-angle ramp. Both mechanisms allow for valid conclusions about the observed deformation, given the chosen boundary conditions, but both also include elements that do not relate to natural fault systems and distort hanging wall geometries and kinematics.

The basal plate model (Fig. 5A; Cloos, 1968; Withjack et al., 1995) uses a thin, commonly rigid, flat plate that underlies some portion of the overlying deformable media. When displaced laterally, the plate imposes a significant velocity and stress discontinuity at the trailing edge that localizes deformation. All active faults are linked to the plate edge. Because the plate is both rigid and unstretchable, most of the hanging wall does not deform. The 'detachment' boundary at the base of the hanging wall has essentially infinite strength. Although gravity drives the faulting above the plate edge, the rigid plate drive itself has no counterpart in nature.

The second method uses a more flexible sheet that underlies some or all of the deformable media (Fig. 5B; McClay and Ellis, 1987; Kerr et al., 1993). The flexibility of the sheet allows for some degree of deformation to conform to the shape of the fault. However, the sheet is also unstretchable, which allows no extension or contraction at the base of the hanging wall. This causes deformation to be minimized near the fault surface, and also induces local contractional structures in some ramp regions (McClay, 1990). Like the basal plate model, the flexible sheet driving forces do not correspond to natural forces.

Lastly, both model techniques are inherently 2-D. Some rigid plate models have used complex shapes for edge geometry and footwall blocks (Xiao and Dula, 1989), and some flexible sheet models have attempted to model deformation above 3-D fault shapes by slicing the sheet into parallel strips (Braun et al., 1994), but in both cases,

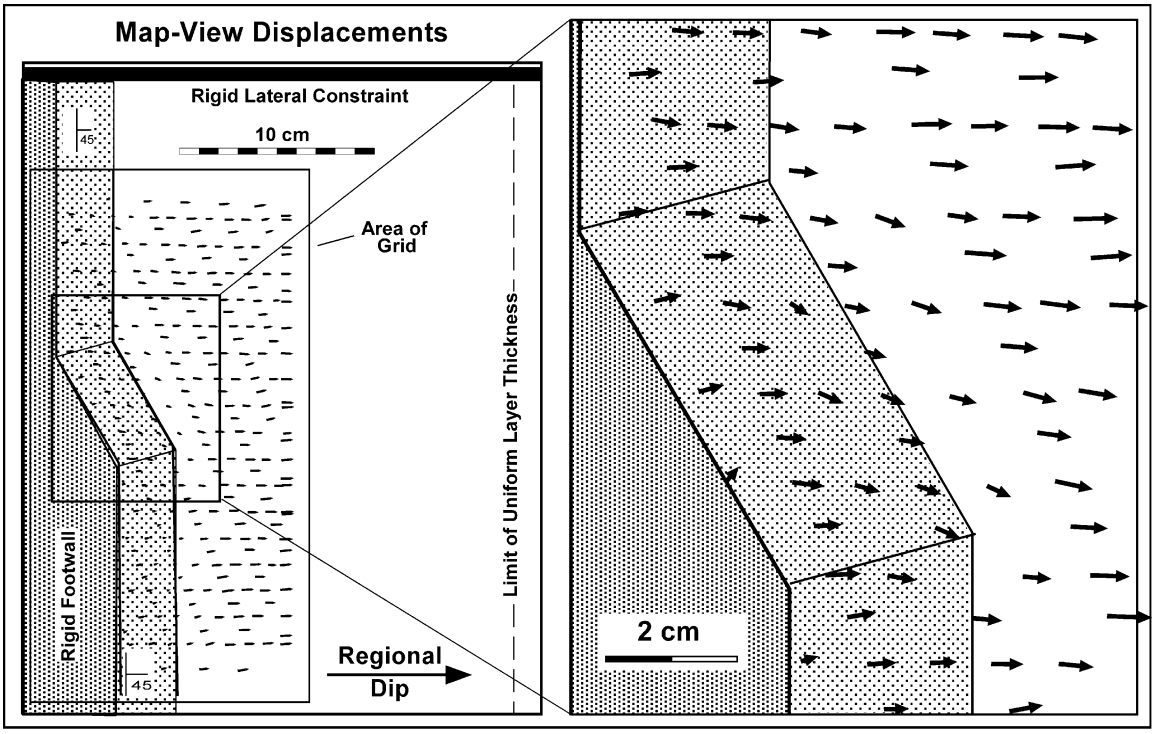


Fig. 7. Map-view displacements of the bent-ramp, weak-fault model in a footwall reference frame. Key features are: (1) rigid motion of bulk hanging wall down the regional dip, and (2) local deflection of the displacement vectors adjacent to the oblique ramp *towards the strike* of the ramp.

deformation in the hanging wall is still constrained by the mechanics of the driving elements, especially the strong boundary at the base of the hanging wall.

### 3.2. Weak fault technique

To overcome some of the limitations of previous models, we use a technique that creates a weak fault zone and relies only on gravity. Thus body forces drive both the fault displacements and the internal deformation of the hanging wall, which can accommodate 3-D strains.

We create a weak fault zone by coating the footwall ramps and flat with a 3-mm-thick layer of silicone putty (Rhone–Poulenc Silbione gomme; Fig. 5C). This particular batch of putty displays somewhat non-Newtonian properties, but at low strain rates has a viscosity of $3 \times 10^4$ Pa-s. The hanging wall consists of about 3 cm of dry, rounded quartz sand (Clemtex #5) with a density of 1.7 g/cc, coefficient of internal friction of 0.9, and minimal cohesive strength (Krantz, 1991).

When assembled, the model is tilted about 3° to induce deformation. Smaller tilt angles may be sufficient, but we did not attempt them. A typical experiment lasted about 2 h, during which time the hanging wall slid down-dip about 6 mm. Within the fault zone, the resulting shear strain rate was about $3 \times 10^{-4}$/s. Based on the viscosity of the putty, the shear stress was about 10 Pa. In contrast, the deviatoric stress required to induce faulting within the base of the sand pack is roughly 200 Pa. Thus, the fault is weaker by a factor of about 20, compared with the sand.

### 3.3. The bent-ramp model and results

Using the weak-fault technique, we modeled the bent-ramp geometry shown in Fig. 2. Model dimensions are 35 cm in the strike direction and 22 cm in the dip direction. The ramp height is 3.2 cm. Rigid walls confine the lateral sides of the model; the resulting boundary effects cause narrow zones of shear that do not extend into the central part of the hanging wall. The down-dip free edge also reveals additional strain, produced by gravitational collapse of the sloping free face of the sand pack. However, this artifact was minimized and isolated from the ramp region by precutting a 20° slope adjacent to the free edge (Fig. 5C).

A passive grid on the surface (Fig. 6A) allowed us to track horizontal displacements, recorded by sequential photographs from a fixed position every 4 min. Comparison of grid nodes yielded displacement vectors (Fig. 7). The sand pack also included passive marker layers of garnet sand. When complete, each experiment was soaked with water and sliced in serial sections to provide views of internal deformation in the final state (Fig. 6B).

Hanging wall deformation typically produces three domains. The bulk of each model deforms by rigid translation down the inclined detachment, except for edge effects (Fig. 7). The second domain includes synthetic and

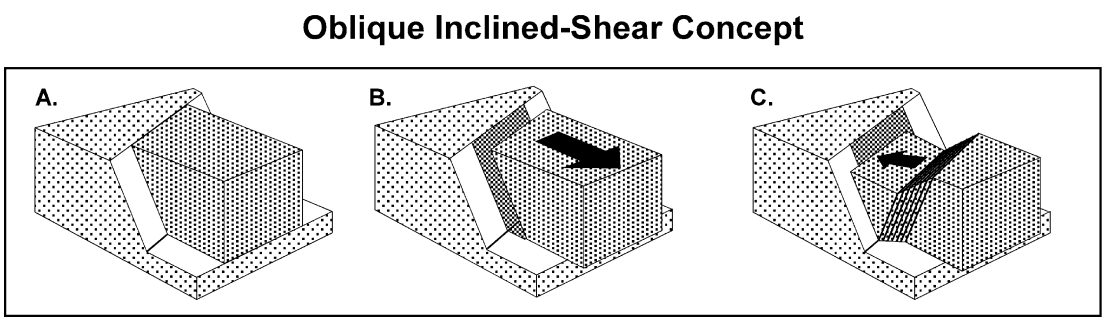


Fig. 8. Oblique inclined-shear model is conceptualized as a two step process. First the hanging wall translates rigidly down the regional dip. This translation opens a void parallel to the fault ramp. Second, gravity drives collapse of the hanging wall normal to the void. The regionally-oblique direction of collapse imparts the out of plane component to the slip.

antithetic faults that develop immediately down-dip of the ramp-flat intersection, and comprise the 'inclined-shear' domain. The third domain includes the material that slid semi-rigidly down the ramps.

Along the sections of the model where the ramp strikes perpendicular to the regional dip, displacement vectors for all three domains point down dip (Fig. 7). In contrast, above the oblique part of the ramp, the vectors are deflected towards the *strike* of the oblique segment. The magnitude of the deflection in the experiment shown varies from 5 to 25°, with an average of 15°. The deflection is greatest near the center of the oblique segment and decreases towards either end. This lateral gradient implies that, at the concave ramp-bend there is a component of horizontal extension perpendicular to regional dip. Similarly, at the convex bend there is a component of horizontal contraction perpendicular to regional dip.

The direction of the deflection in the oblique-ramp region and lateral-strain distributions are opposite to our intuitive expectations. We had expected a local down-dip component above the oblique ramp, leading to a deflection toward the local *dip* direction. To explain this, we develop a geometric model that generalizes inclined shear to three dimensions.

## 4. Oblique-inclined theory

### 4.1. Derivation

The model is conceptually equivalent to 2-D, inclined-shear models in which the hanging wall is imagined to pull rigidly away from the footwall and then to collapse into the resulting void (Fig. 8). The geometry of the fault bend requires a kinematic system that includes shear along planes

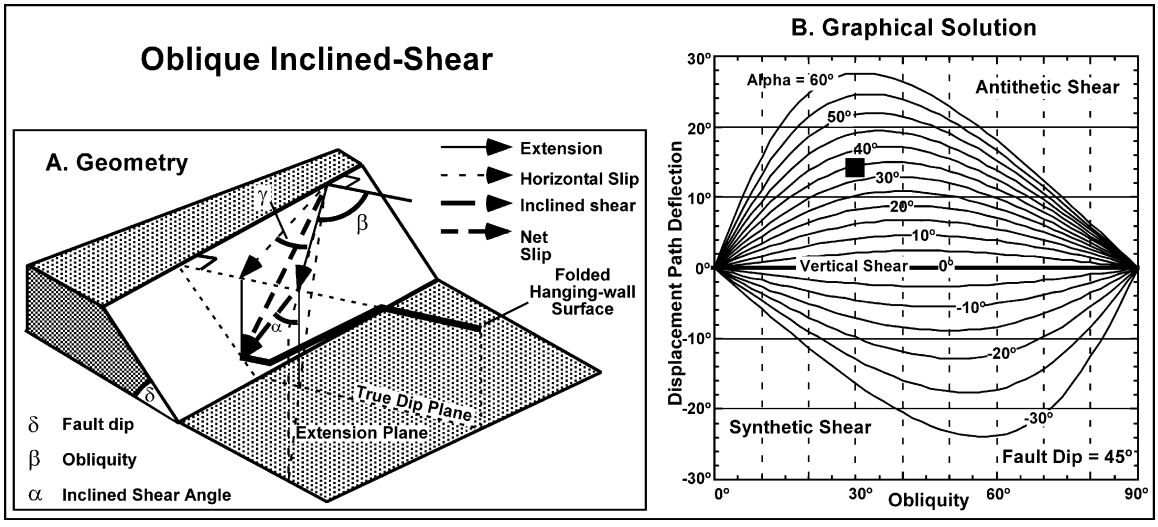


Fig. 9. (A) Analytical relationship is derived from the geometry of oblique inclined shear. Two vertical planes are key: (1) the extension plane that contains the extension vector, and (2) the true dip plane that is perpendicular to the fault ramp. Three angular parameters control the out-of-plane slip component. The obliquity ($\beta$) is the angle between the extension direction and the normal to the ramp strike. The dip of the fault plane is $\delta$. The inclined-shear angle ($\alpha$) is measured from the intersection of the two vertical planes. From these three parameters, the map-view deflection ($\gamma$) of the slip vector from the extension direction is determined. (B) Graphical solution of the inclined-shear equation for a constant fault dip of 45°. Solution is plotted as curves of constant inclined-shear angle. Negative shear angles represent synthetic shear. Note that antithetic shear produces strike-parallel deflection, vertical shear produces no deflection, and synthetic slip produces strike-perpendicular deflection. Parameters of the study are indicated by the square.

Table 2
Specified, measured, and calculated model parameters for testing oblique inclined-shear theory

| Experiment | Specified | | Measured | Calculated from theory |
|---|---|---|---|---|
| | Fault dip (°) | Obliquity (°) | Deflection (°) | Effective inclined-shear angle (°) |
| *Extensional sand* | | | | |
| This study | 45 | 30 | 14.7 | 34 |
| *Extensional clay* | | | | |
| Dula and Xiao 1 | 30 | 0 | 0.5 | na |
| Dula and Xiao 2 | 30 | 30 | 5 | 20 |
| Dula and Xiao 3 | 33 | 30 | 3.5 | 13 |
| Dula and Xiao 4 | 33 | 60 | 4 | 15.5 |
| *Compressional sand* | | | | |
| Wilkerson et al. 1 | 20 | 30 | 4 | 25 |
| Wilkerson et al. 2 | 20 | 50 | 4 | 24 |
| Wilkerson et al. 3 | 30 | 30 | 6.5 | 26 |
| Wilkerson et al. 4 | 30 | 50 | 6 | 23 |

that contain the ramp–flat intersection line (Suppe, 1983; Hardy, 1995). In this case, the line is parallel to the fault strike.

Although synthetic and vertical shear are geometrically possible, antithetic shear is observed. The antithetic shear is normal to the incipient void (i.e. perpendicular to the fault trace), thus introducing a component of slip normal to the local fault strike (Fig. 8). Vector sum of the normal component with the regional component results in the observed displacement paths.

From the geometry of the conceptual model (Fig. 9A), an analytical relationship can be derived in three dimensions, which predicts the deflection of particle motion from the regional dip direction. This relationship, derived in the appendix, is presented here as Eq. (2). Eq. (2) shows that the deflection angle ($\gamma$) is a function of three parameters: fault dip ($\delta$), ramp obliquity ($\beta$), and the *effective* inclined-shear angle ($\alpha$):

$$\gamma = 90 - \beta - \tan^{-1}\left(\cot\beta\left[1 - \frac{\sin\delta\sin\alpha}{\cos(\delta - \alpha)}\right]\right) \quad (2)$$

Fig. 9B shows this solution graphically for the case of a 45° ramp. The graph shows three key features of the relationship: (1) $\gamma$ is zero if $\beta$ is zero (2-D case), (2) $\gamma$ is zero if $\alpha$ is zero (vertical-shear case), and (3) antithetic and synthetic shear create opposite senses of deflection.

### 4.2. Comparison with previous work

Apotria et al. (1992) developed similar kinematic models of deformation at an oblique ramp. Rather than using arbitrarily inclined shear, these authors modeled compressional ramps using vertical and layer-parallel shear. In fact, both of these cases can be treated as special cases of the oblique inclined shear.

Vertical shear can clearly be treated by setting $\alpha = 0$. Less obvious is that the layer-parallel shear case is equivalent to inclined shear where the shear plane bisects the dihedral angle between the folded bedding (Hardy, 1995). The specific angle required is a function of the fault-cutoff angles and can be calculated using trigonometric (Suppe, 1983) or algebraic formulations (Hardy, 1995).

### 4.3. Evaluation

Of the four parameters in the theory, two (fault dip and obliquity) are known model boundary conditions, one (deflection) is measurable, and one (inclined-shear angle) is unknown. In fact, the inclined-shear angle is an abstract model concept and cannot be measured. Were hanging wall deformation to occur by slip on closely spaced planes with uniform direction, we might directly measure the orientations of these slip planes. However, even in these relatively simple models, deformation occurs on a more complex array of slip planes. Thus, the inclined-shear angle is more precisely an *effective inclined-shear angle,* which is related to the net movement of the complex system. Given this complexity, a precise test of the theory is not possible. Instead, we use the three known and measured parameters to calculate the inclined-shear angle. By comparing the calculated values with similar experiments, we test the theory's consistency and predictive value.

We use three sets of analog models for our comparison:

1. the oblique-ramp, weak fault model (this study),
2. four stiff-sheet extensional clay models by Xiao and Dula (1989), and
3. four dry sand compressional models by Wilkerson et al. (1992).

The model parameters and results are summarized in Table 2.

For this study $\delta = 45°$, $\beta = 30°$, and $\gamma$, varied from 5 to 25° with an average of 15° (Fig. 7). For these values, $\alpha$ is predicted to be 34°, which corresponds to a fault dip of 56°

(Fig. 9B). Individual faults observed in the bent fault model are considerably steeper that this prediction. However, this dip closely approximates that of the down-dip boundary of the zone of hanging wall faulting.

Xiao and Dula (1989) performed a series of four extensional ramp analog models using a similar bent ramp model. They used a stiff-sheet drive and a wet clay hanging wall over a rigid footwall with smooth strike bends. A range of model parameters were used: $\delta = 30–33°$, $\beta = 0$, 30, and 60°, $\gamma = 3.5–5°$. Predicted $\alpha$ values range from 13 to 20°, which is typical for wet clay experiments (Dula, 1991).

Wilkerson et al. (1992) performed oblique-ramp compressional experiments with dry sand. They observed an equivalent deflection of particle motion adjacent to the oblique ramp. Parameters in their models were: $\delta = 20$ and 30°, $\beta = 30$ and 50°, and $\gamma = 4–6°$. Predicted $\alpha$ values cluster tightly from 23 to 26°, similar to values for equivalent extensional, dry-sand experiments (Kerr and White, 1992).

From these examples, the oblique inclined-shear model appears to be applicable in both compression and extension across a range of model parameters and material properties. This is so because the model is based on the geometry of the fault bend. Therefore, so long as the hanging wall deformation is homogeneous, it is this geometry that dominantly controls the material displacements adjacent to fault bends.

### 4.4. Implications

Lateral deflection of particle motion at 3-D fault bends potentially impacts the conventional assumption of plane strain used in 2-D cross-section construction and restoration. However, inspection of Fig. 9B reveals that the deflection magnitudes are generally low. For the 45° case, typical inclined-shear values of 10–30° (Dula, 1991) result in maximum lateral deflections of 4–14°. For a given fault dip, the maximum deflection values occur at fault obliquity angles of 30–60°. As fault bends angles approach 0 or 90°, lateral deflections rapidly approach 0° (Fig. 9B). For the purpose of cross-section balancing, lateral displacements less than 10° are generally considered acceptable (Woodward et al., 1985). Thus, only rarely would we expect oblique-shear processes to be a significant factor for cross-section construction.

Perhaps of more importance are implications for distributed strain at 3-D fault bends. Eq. (2) predicts convergent flow at convex bends and divergent flow at concave bends. This counter-intuitive pattern is observed in the sand model (Fig. 7). This non-parallel flow is presumably accommodated by increased vertical and/or volumetric strains at the fault bends. We would expect such strains to be dilatational at concave bends and compressive at convex bends. Whether or not these strains materially impact fluid flow, rheology, or other fault zone properties is unknown.

## 5. Conclusions

From this study we make four main conclusions.

1. Along-strike changes in fault shape can generate local structural highs and lows and produce lateral fold closure in the presence of a regional dip.
2. Fault heave varies as the fault strike and dip change and bears no clear relationship to the true slip. Matching of characteristic shapes between hanging wall and footwall indicates the true slip.
3. A component of strike-parallel motion adjacent to oblique ramps is observed in this and other studies. The oblique-inclined shear model, based on geometric analysis, explains this observed motion. The quantitative theory reduces to the planar 2-D solution in the orthogonal and vertical shear cases. Predicted 3-D strains are generally small. We would expect them to rarely be a significant factor for cross-section construction.
4. The weak-fault analog-modeling technique provides a less restrictive and more natural drive mechanism than the basal plate or flexible sheet techniques commonly used for modeling extensional ramp systems.

## Acknowledgements

We thank ARCO management for support for this research and for permission to publish it. This study benefited from many active discussion sessions and constructive criticism by the ARCO Structural Geology group. Jennifer Winkler digitized the analog model displacement paths. Several members of the ARCO Exploration and Production Technology drafting department contributed to various figures. Finally, we thank Bruno Vendeville, Ted Apotria, and an anonymous reviewer for constructive criticism, which improved the manuscript. Also we thank ChevronTexaco Exploration and Production Technology Company for paying the color printing charges.

## Appendix A. Derivation of oblique inclined-shear

We derive Eq. (2) for oblique inclined shear from the geometry of the fault and from the assumed deformation mechanism. Fig. A1 and Table A1 show the geometry of the fault and define angles and distances used in the derivation. Note that we designate points with lower case letters, distances and vectors with capital letters, and angles with Greek letters. We assume that the hanging wall deformation due to motion over an oblique fault can be divided into two discrete steps:

1. a rigid translation parallel to the regional extension direction

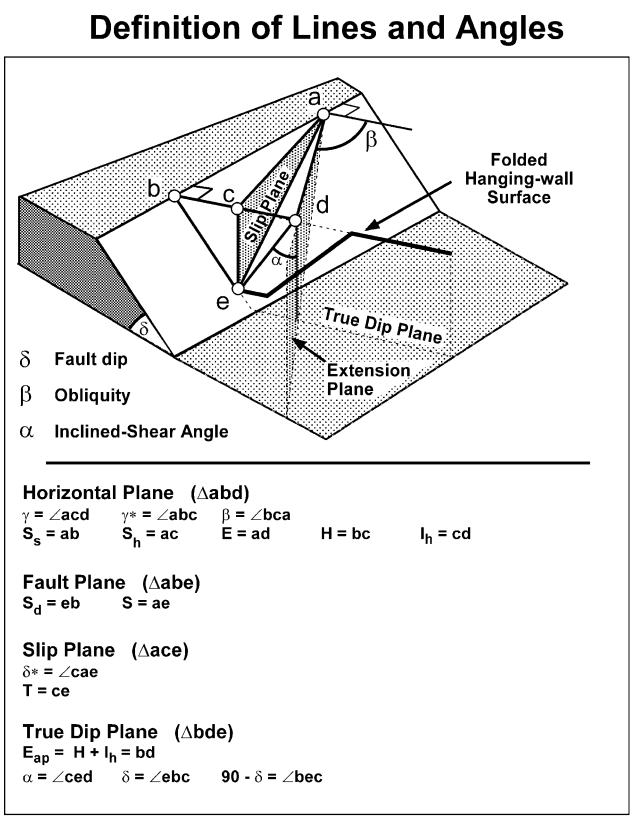


Fig. A1.

2. inclined shear in a plane perpendicular to the strike of the local fault segment.

Our goal is to determine the throw ($T$), horizontal slip ($S_h$), and the angle between horizontal slip and extension directions ($\gamma$) in terms of the extension vector ($E$), fault dip ($\delta$), inclined-shear angle ($\alpha$), and obliquity ($\beta$).

We do this in four steps: some preliminary derivations, a solution for $T$, a solution for $S_h$ (in terms of $\gamma$), and finally a solution for $\gamma$.

### A.1. Preliminary derivations

From definition of $\beta$:

$$E_{ap} = E\cos\beta \tag{A1}$$

Law of sines yields:

$$\frac{\sin\delta}{I} = \frac{\sin(90-\delta+\alpha)}{E_{ap}}$$

$$\frac{\sin\delta}{I} = \frac{\sin(90-(\delta-\alpha))}{E_{ap}}$$

$$I = \frac{E_{ap}\sin\delta}{\cos(\delta-\alpha)} \tag{A2}$$

Table A1
Definition of parameters used to derive Eq. (2) (see Fig. A1)

| | |
|---|---|
| $E$ | Extension vector |
| $E_{ap}$ | Apparent extension (horizontal component in dip direction) |
| $S$ | Net slip |
| $S_h$ | Horizontal slip |
| $S_d$ | Dip slip |
| $S_s$ | Strike slip |
| $I$ | Inclined-shear displacement |
| $I_h$ | Horizontal component of inclined-shear displacement |
| $H$ | Heave |
| $T$ | Throw (equals vertical slip or vertical component of inclined-shear displacement) |
| $\alpha$ | Inclined-shear angle |
| $\beta$ | Obliquity |
| $\gamma$ | Angle between horizontal slip and extension directions |
| $\gamma*$ | Angle between fault strike and horizontal slip direction |
| $\delta$ | Fault dip |
| $\delta*$ | Apparent fault dip in horizontal slip direction |

Combining Eqs. (A1) and (A2):

$$I = \frac{E\cos\beta\sin\delta}{\cos(\delta-\alpha)}$$

Note: same as 2-D when $\beta = 0$.

Similarly:

$$\frac{\sin(90-\alpha)}{S_d} = \frac{\sin(90-\delta+\alpha)}{E_{ap}}$$

$$S_d = \frac{E\cos\beta\cos\alpha}{\cos(\delta-\alpha)} \tag{A3}$$

By definition:

$$H = E_{ap} - I_h \tag{A4}$$

From elementary trigonometry:

$$I_h = I\sin\alpha = T\tan\alpha \tag{A5}$$

$$T = H\tan\delta \tag{A6}$$

and

$$S_s = E\sin\beta \tag{A7}$$

From triangles $\Delta S_s H S_h$ and $\Delta I_h S_h E$

$$\gamma = 90 - \left(\beta + \tan^{-1}\left[\frac{H}{S_s}\right]\right) \tag{A8}$$

Law of sines for triangle $\Delta S_h E I_h$:

$$S_h = \frac{I_h\sin\beta}{\sin\gamma} \tag{A9}$$

### A.2. Solution for T

Substitution of Eqs. (A1), (A2), (A4), and (A5) into

Eq. (A6) gives:

$$T = \left(E\cos\beta - \left[\frac{\sin\delta\sin\alpha E\cos\beta}{\cos(\delta-\alpha)}\right]\right)\tan\delta$$

$$T = E\cos\beta\tan\delta\left[1 - \frac{\sin\delta\sin\alpha}{\cos(\delta-\alpha)}\right] \quad \text{(A10a)}$$

Alternately, from triangle $\Delta ITI_h$:

$$T = I\cos\alpha$$

Substituting Eq. (A2):

$$T = \frac{E\cos\beta\sin\delta\cos\alpha}{\cos(\delta-\alpha)} \quad \text{(A10b)}$$

Eqs. (A10a) and (A10b) can be shown to be identical using the laws of trigonometric sums.

*A.3. Solution for $S_h$ (in terms of $\gamma$):*

Substitution of Eqs. (A5) and (A10b) into Eq. (A9) gives:

$$S_h = T\tan\alpha\left[\frac{\sin\beta}{\sin\gamma}\right]$$

$$S_h = \left[\frac{E\cos\beta\sin\delta\cos\alpha}{\cos(\delta-\alpha)}\right]\tan\alpha\left[\frac{\sin\beta}{\sin\gamma}\right]$$

$$S_h = \frac{E\cos\beta\sin\delta\cos\alpha\tan\alpha\sin\beta}{\cos(\delta-\alpha)\sin\gamma}$$

$$S_h = E\left[\frac{\sin\delta\sin\alpha\cos\beta\sin\beta}{\cos(\delta-\alpha)\sin\gamma}\right] \quad \text{(A11a)}$$

Alternately, elementary trigonometry yields:

$$S_h = \frac{S_s}{\cos(\gamma^*)}$$

Substitution of Eq. (A7) gives:

$$S_h = \frac{E\sin\beta}{\cos(\gamma^*)}$$

From triangle $\Delta EE_{ap}S_s$:

$$\gamma^* + \gamma + \beta = 90 \text{ or } \gamma^* = 90 - (\gamma + \beta)$$

Thus:

$$S_h = \frac{E\sin\beta}{\sin(\gamma+\beta)} \quad \text{(A11b)}$$

*A.4. Solution for $\gamma$*

Substitution of Eqs. (A1), (A2), (A4), and (A7) into Eq. (A8) gives:

$$\gamma = 90 - \left(\beta + \tan^{-1}\left[\frac{E\cos\beta - \sin\delta\left\{\frac{E\cos\beta}{\cos(\delta-\alpha)}\right\}\sin\alpha}{E\sin\beta}\right]\right)$$

$$\gamma = 90 - \left(\beta + \tan^{-1}\left[\frac{\cos\beta - \sin\delta\sin\alpha\left\{\frac{\cos\beta}{\cos(\delta-\alpha)}\right\}}{\sin\beta}\right]\right)$$

$$\gamma = 90 - \beta - \tan^{-1}\left[\cot\beta - \frac{\sin\delta\sin\alpha\cot\beta}{\cos(\delta-\alpha)}\right]$$

$$\gamma = 90 - \beta - \tan^{-1}\left(\cot\beta\left[1 - \frac{\sin\delta\sin\alpha}{\cos(\delta-\alpha)}\right]\right) \quad \text{(A12)}$$

## References


Apotria, T.G., Snedden, W.T., Spang, J.H., Wiltschko, D.V., 1992. Kinematic models of deformation at an oblique ramp. In: McClay, K. (Ed.). Thrust Tectonics. Chapman & Hall, London, pp. 141–154.

Braun, J., Batt, G.E., Scott, D.L., McQueen, H., Beasley, A.R., 1994. A simple kinematic model for crustal deformation along two- and three-dimensional listric normal faults derived from scaled laboratory experiments. Journal of Structural Geology 16, 1477–1490.

Cloos, E., 1968. Experimental analysis of Gulf Coast fracture patterns. American Association of Petroleum Geologists Bulletin 52, 420–444.

Dula Jr, W.F., 1991. Geometric models of listric normal faults and rollover folds. American Association of Petroleum Geologists Bulletin 75, 1609–1625.

Hardy, S., 1995. A method for quantifying the kinematics of fault-bend folding. Journal of Structural Geology 17, 1785–1788.

Kerr, H.G., White, N., 1992. Laboratory testing of an automatic method for determining normal fault geometry at depth. Journal of Structural Geology 14, 873–885.

Kerr, H.G., White, N., Brun, J.-P., 1993. An automatic method for determining three-dimensional normal fault geometries. Journal of Geophysical Research 98, 17,837–17,857.

Krantz, R.W., 1991. Measurements of friction coefficients and cohesion for faulting and fault reactivation in laboratory models using sand and sand mixtures. Tectonophysics 188, 203–207.

McClay, K.R., 1990. Deformation mechanics in analogue models of extensional fault systems. In: Rutter, E.H., Knipe, R.J. (Eds.), Deformation Mechanisms, Rheology and Tectonics. Geological Society of London, Special Publication 54, pp. 445–454.

McClay, K.R., Ellis, P.G., 1987. Geometries of extensional fault systems developed in model experiments. Geology 15, 341–344.

Suppe, J., 1983. Geometry and kinematics of fault-bend folding. American Journal of Science 283, 684–721.

White, N.J., Jackson, A., McKenzie, D., 1986. The relationship between the geometry of normal faults and that of the sedimentary layers in their hanging walls. Journal of Structural Geology 8, 897–909.

Wilkerson, M.S., Marshak, S., Bosworth, W., 1992. Computerized tomographic analysis of displacement trajectories and three-dimensional fold geometry above oblique thrust ramps. Geology 20, 439–442.

Withjack, M.O., Islam, Q.T., La Point, P.R., 1995. Normal faults and their hanging-wall deformation: an experimental study. American Association of Petroleum Geologists Bulletin 79, 1–18.

Woodward, N.B., Boyer, S.P., Suppe, J., 1985. An Outline of Balanced Cross-Sections. Studies in Geology, 11. University of Tennessee, Department of Geological Sciences, 170pp.

Xiao, H., Dula, W.F., Jr., 1989. Three- and two-dimensional clay modelling of hanging-wall deformation above detached normal faults. Unpublished ARCO Exploration Research and Technical Services, Summer-intern research report.

Xiao, H., Suppe, J., 1992. Origin of rollover. American Association of Petroleum Geologists Bulletin 76, 509–529.